ELSEVIER

Contents lists available at ScienceDirect

# Colloids and Surfaces A: Physicochemical and Engineering Aspects





# Accelerating proton-coupled electron transfer: Defect-rich cobalt-decorated crystalline/amorphous Co<sub>2</sub>B-MoB<sub>2</sub>/CMO heterointerface catalysts for enhanced NaBH<sub>4</sub> hydrolysis

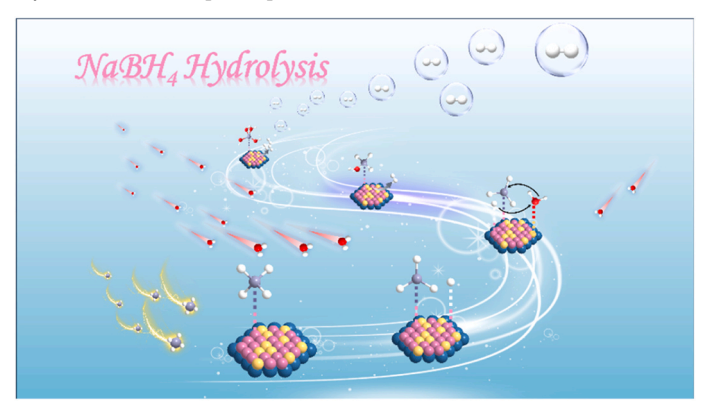
Luyan Shi <sup>a,1</sup>, Chenxi Shang <sup>a,1</sup>, Ke Zhu <sup>a</sup>, Fengli Wei <sup>a</sup>, Bin Wu <sup>c,\*</sup>, Tayirjan Taylor Isimjan <sup>b,\*</sup>, Xiulin Yang <sup>a,\*</sup>

#### HIGHLIGHTS

- The catalyst exhibits a high HGR (7364.3 mL min<sup>-1</sup> g<sup>-1</sup>) and multi-cycle reusability.
- The synergy between crystalline and amorphous phases, coupled with rich Co defects, dominates the high hydrolysis activity.
- The generated hydrogen successfully powered an H<sub>2</sub>-air fuel cell and lit up a small light bulb.

#### GRAPHICAL ABSTRACT

A crystalline/amorphous  $Co_2B\text{-}MoB_2/CMO$  heterointerface catalyst was synthesized via chemical coprecipitation and sodium borohydride reduction methods. The optimized catalyst exhibited a high hydrogen production rate of 7364.3 mL min<sup>-1</sup> g<sup>-1</sup> at 298 K. The superior catalytic activity of  $Co_2B\text{-}MoB_2/CMO$  is primarily attributed to abundant defect sites and strong synergistic interactions between the crystalline and amorphous phases.



#### ARTICLE INFO

Keywords: Co<sub>2</sub>B-MoB<sub>2</sub>/CMO Crystalline/amorphous Heterointerface Cobalt defects NaBH<sub>4</sub> hydrolysis

#### ABSTRACT

The development of efficient and long-lasting catalysts for hydrogen generation is vital for advancing innovations in clean energy technologies. In this study, we synthesized and characterized  $\text{Co}_2\text{B-MoB}_2/\text{CMO}$ , a crystalline/amorphous heterointerface catalyst, for sodium borohydride (NaBH<sub>4</sub>) hydrolysis, achieving a high hydrogen generation rate of 7364.3 mL min<sup>-1</sup> g<sup>-1</sup> at 298 K. The activation energy of 44.4 kJ mol<sup>-1</sup> was lower than that of most reported catalyst. Both experimental and theoretical analyses demonstrate that Co defects and the interfacial regions between crystalline and amorphous phases in  $\text{Co}_2\text{B-MoB}_2/\text{CMO}$  are essential in integrating critical

E-mail addresses: bin.wu@ntu.edu.sg (B. Wu), isimjant@sabic.com (T.T. Isimjan), xlyang@gxnu.edu.cn (X. Yang).

a Guangxi Key Laboratory of Low Carbon Energy Materials, School of Chemistry and Pharmaceutical Sciences, Guangxi Normal University, Guilin 541004, China

b Saudi Arabia Basic Industries Corporation (SABIC) at King Abdullah University of Science and Technology (KAUST), Thuwal 23955-6900, Saudi Arabia

<sup>&</sup>lt;sup>c</sup> School of Materials Science and Engineering, Nanyang Technological University, 50 Nanyang Avenue, Singapore 639798, Singapore

<sup>\*</sup> Corresponding authors.

 $<sup>^{1}</sup>$  Contributed equally to this work.

factors, such as a high concentration of unsaturated coordination sites. These features not only alter the surface electronic properties but also enhance the adsorption of  $H_2O$  molecules and promote the dissociation of the  $BH_4^-$ , thereby optimizing catalytic performance. In addition, the NaBH4 hydrolysis hydrogen production system based on this catalyst successfully drove a hydrogen-air fuel cell and lit up a small light bulb, demonstrating its potential in practical applications.

#### 1. Introduction

Hydrogen (H2) is widely regarded as a green energy carrier, but its utilization through most existing production technologies requires storage, which involves compression and shipping [1,2]. Hydrogen is typically transported either as a compressed gas (20-70 MPa) or as a cryogenic liquid at 20 K, both of which present significant challenges in terms of cost and safety. Therefore, direct hydrogen production at refueling stations or chemical plants could offer a more viable solution for future hydrogen applications [3]. Sodium borohydride (NaBH<sub>4</sub>) hydrolysis presents a promising alternative, as it eliminates the need for complex storage infrastructure and enables on-demand hydrogen production, effectively addressing many of the issues associated with hydrogen storage and transportation. This makes NaBH<sub>4</sub> an attractive option for portable applications [4]. For instance, Hsueh et al. [5] prepared a solid mixture comprising NaBH<sub>4</sub>, Co<sup>2+</sup>/IR-120, and silicone rubber that generated hydrogen at a rate of 25 mL/min for two hours, successfully powering a 2 W proton exchange membrane fuel cell (PEMFC) without requiring external heating. Similarly, Li et al. [6] created a system using cobalt oxide and nickel foam that produced hydrogen at 30 SLPM to power a 3 kW PEMFC. However, the slow hydrogen production rate from the direct reaction of NaBH4 with water typically requires the addition of transition metal catalysts or acids to enhance the hydrolysis process [7,8].

Various catalytic systems, including noble metals (e.g., Rh [9], Ru [10] Pt [11] and Pd [12] and non-noble metals (e.g., Fe, Co, Ni, and Cu), have been explored for hydrogen production. Although noble metal nano-catalysts demonstrate excellent catalytic activity, their high cost and limited supply present considerable obstacles for widespread industrial use [13]. Consequently, recent efforts have focused on developing noble-metal-free catalysts with noble-like activity for hydrogen evolution from sodium borohydride. These include earth-abundant transition metal oxides [14], alloys [15,16], boride [17], nitrides [18], and phosphides [19]. Among these, transition metal borides have shown great potential as catalysts for sodium borohydride hydrolysis due to their excellent electrical conductivity, high intrinsic catalytic activity, and accessibility. Elemental boron, the smallest metal-like element, possesses unique physicochemical properties, such as a small atomic radius and high electronegativity, making it prone to forming covalent compounds with metallic characteristics [20]. However, previous research has demonstrated that unsupported boride nanoparticle catalysts are prone to aggregation due to their high surface energy and magnetic interactions. This aggregation can hinder the hydrogen production rate and shorten the catalyst's lifespan [21]. One effective strategy to address this aggregation issue is using a high-surface-area growth substrate to enhance the dispersion of CoB particles [22]. CoMoO<sub>4</sub> is widely employed as a catalyst substrate, effectively preventing particle aggregation and improving catalytic activity [23]. Notably, incorporating Mo into Co-based catalysts provides distinct advantages in modulating catalytic performance. The exceptional redox ability of Co, combined with the high conductivity of Mo, enables synergistic effects that enhance catalytic efficiency [24].

Among recent advancements, phase engineering of crystalline/amorphous heterostructured nanomaterials has proven to be a practical approach for enhancing catalytic properties [25]. For example, Liang et al. developed a NiB/NiFe<sub>2</sub>O<sub>4</sub> catalyst with a crystalline/amorphous heterojunction structure for sodium borohydride hydrolysis, significantly improving hydrogen production efficiency, with a reported

hydrogen evolution rate of 299.88 mL min<sup>-1</sup> g<sup>-1</sup> [26]. The enhanced performance can be attributed to the cooperative effects arising from the coexistence of crystalline and amorphous domains. The amorphous phase contributes additional active sites and enhances charge transfer, while the crystalline phase maintains structural stability and supports efficient electron transport [27]. Defect engineering has become a promising approach to enhance catalytic performance by altering the electronic structure of catalysts [28]. For instance, Shang et al. reported a Co<sub>2</sub>B-MoO<sub>3</sub>/MOF heterojunction catalyst with cobalt defects that exhibited remarkable performance in NaBH<sub>4</sub> hydrolysis. The introduction of cobalt defects increased the number of active sites and optimized the electronic structure around these sites, facilitating the adsorption and activation of BH<sub>4</sub> and H<sub>2</sub>O molecules [29]. The presence of cobalt defects thus provides a flexible platform for tuning the electronic structure and enhancing catalytic efficiency in hydrogen generation from NaBH<sub>4</sub> hydrolysis.

Building on these insights, we have successfully synthesized crystalline/amorphous Co<sub>2</sub>B-MoB<sub>2</sub>/CMO heterointerface catalysts enriched with cobalt defects using a chemical co-precipitation method followed by sodium borohydride reduction treatment. During boronization, boron atoms are incorporated into the CoMoO6 matrix, forming an amorphous layer around the free-standing, interconnected nanorods. A thorough range of characterization methods has been utilized to examine the crystallinity, microstructure, porosity, and chemical states of the different components. Based on the Michaelis-Menten model, we propose a catalytic mechanism for NaBH<sub>4</sub> hydrolysis using the Co<sub>2</sub>B-MoB<sub>2</sub>/CMO system. As expected, Co<sub>2</sub>B and MoB<sub>2</sub> in Co<sub>2</sub>B-MoB<sub>2</sub>/CMO effectively activate BH<sub>4</sub> and H<sub>2</sub>O, respectively, facilitating the hydrolysis process. The optimized Co<sub>2</sub>B-MoB<sub>2</sub>/CMO catalyst demonstrates remarkable activity in alkaline sodium borohydride solutions, underscoring its potential for use in energy storage and conversion applications.

### 2. Experimental section

#### 2.1. Materials

Cobalt chloride hexahydrate (CoCl $_2$ -6 H $_2$ O, 99.0 %, Aladdin), sodium molybdate dihydrate (Na $_2$ MoO $_4$ -2 H $_2$ O, 99 %, Xilong Scientific), acetone (CH $_3$ CoCH $_3$ , 99.5 %, Xilong Scientific), sodium chloride (NaCl, 99.5 %, Xilong Scientific), sodium hydroxide (NaOH, 96 %, Aladdin), urea (H $_2$ NCONH $_2$ , 99.0 %, Xilong Scientific), sodium borohydride (NaBH $_4$ , 98.0 %, Sinopharm Group), ethanol (99.7 %, Xilong Scientific). The study utilized commercially available analytical-grade reagents and solvents, which were used directly without further purification. The deionized water (18.2 M $\Omega$  cm $^{-1}$ ) from a UPTA-20 water purification system (China Shanghai Lichen Bangxi Instrument Technology Co., Ltd.) was used throughout the experiment. All chemical reagents were obtained commercially in analytical purity and utilized directly without further processing.

### 2.2. Synthesis of CoMoO<sub>6</sub>·0.9 H<sub>2</sub>O (CMO) nanorods

The CoMoO $_6\cdot0.9$  H $_2$ O (CMO) nanorods were prepared using a water bath process reported in the previous work with slight modification [30]. Typically, 5 mmol CoCl $_2\cdot6$  H $_2$ O and Na $_2$ MoO $_4\cdot2$  H $_2$ O were dissolved in 30 mL H $_2$ O. Then, the Na $_2$ MoO $_4\cdot2$  H $_2$ O solution was added dropwise to the CoCl $_2\cdot6$  H $_2$ O solution and stirred at 70 °C for 2 h. The

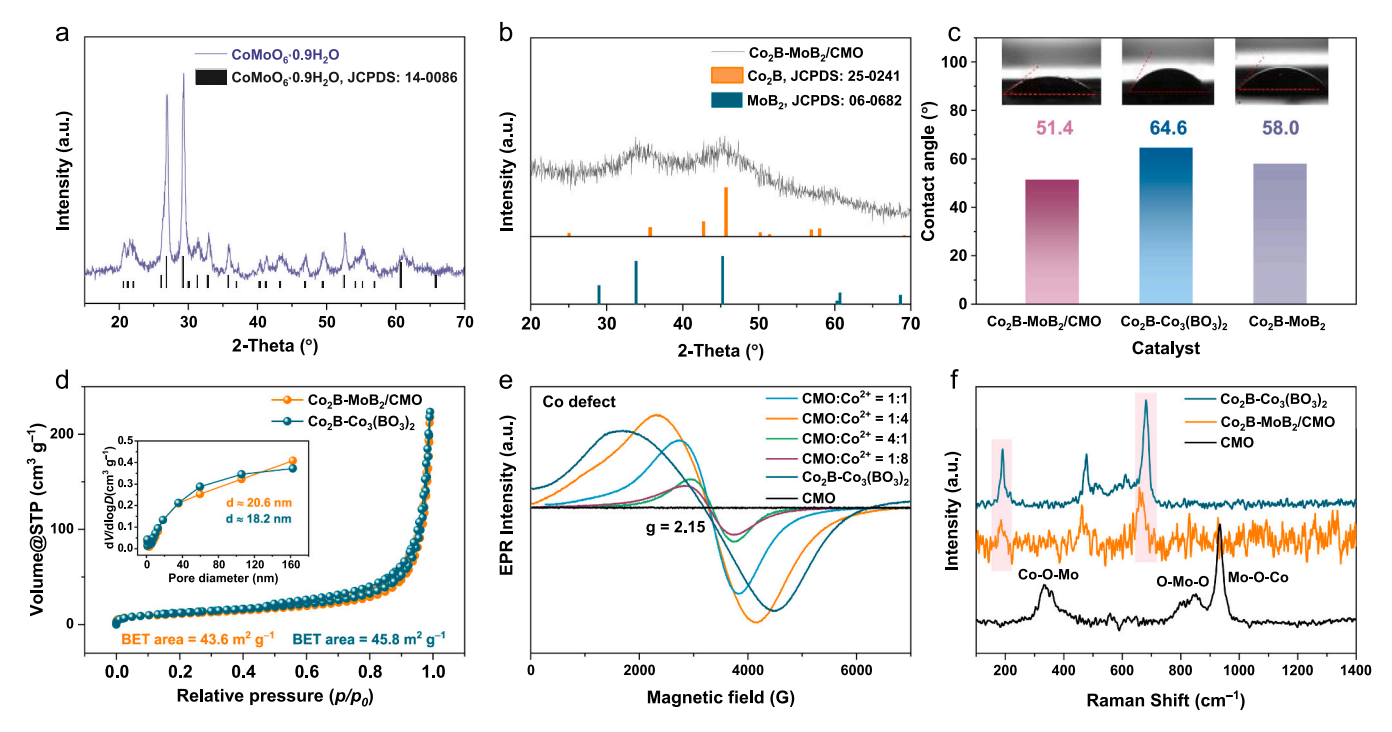


Fig. 1. (a) XRD pattern of  $CoMoO_6$ -0.9  $H_2O$  (CMO). (b) XRD pattern of  $Co_2B$ -Mo $B_2$ /CMO. (c) Bubble contact angle images of different catalysts. (d)  $N_2$  adsorption—desorption isotherm with the inset showing the corresponding pore size distribution of  $Co_2B$ -Mo $B_2$ /CMO and  $Co_2B$ -Co $_3$ (BO $_3$ ) $_2$ . (e) EPR spectra of the catalysts. (f) Raman spectra of  $Co_2B$ -Mo $B_2$ /CMO,  $Co_2B$ -Co $_3$ (BO $_3$ ) $_2$  and CMO.

synthesized solid was subjected to extensive purification through sequential washing with large volumes of deionized water and anhydrous ethanol. Subsequently, the purified product was oven-dried at 60 °C for 12 h to remove residual solvents.

# 2.3. Synthesis of CMO-Co<sup>2+</sup>

30 mg of CMO and 120 mg of CoCl $_2$ -6 H $_2$ O were ultrasonically dispersed into 10 mL of acetone. The reaction system was continuously agitated using a magnetic stirrer at room temperature until visual confirmation of complete solvent removal was achieved. The resulting solid residue was then carefully harvested using a spatula and stored in a desiccator for subsequent characterization. To compare the performance of different Co $^{2+}$  doping levels, the CMO/CoCl $_2$ -6 H $_2$ O mass ratio was varied (1:1, 1:4, 1:8, 4:1) during the synthesis process.

#### 2.4. Synthesis of Co<sub>2</sub>B-MoB<sub>2</sub>/CMO

The 50 mg CMO-Co $^{2+}$  were ground with 1 g NaCl and 1 g urea, the resulting powder was subsequently transferred to a glass container and subjected to thermal treatment at 60 °C for 4 h. The dried precursor was mixed with different amounts (0.1 g, 0.2 g and 0.3 g) of NaBH4, stirred uniformly with a weighing spoon, and left to ensure a complete solid-state reaction. The synthesized product was isolated through centrifugal separation, followed by sequential purification using distilled water and anhydrous ethanol. Final drying was performed under vacuum conditions at 70 °C for a duration of 12 h. The Co $_2$ B-Co $_3$ (BO $_3$ ) $_2$  material without CMO was also prepared.

Material characterizations and catalytic hydrolysis of NaBH<sub>4</sub> measurements are described explicitly in Supporting Information.

### 3. Results and discussion

### 3.1. Synthesis and characterization

The X-ray diffraction (XRD) pattern of CoMoO<sub>6</sub>·0.9 H<sub>2</sub>O (CMO)

(Fig. 1a) confirms its successful synthesis, exhibiting well-defined crystalline peaks indexed to JCPDS: 14-0086. In Fig. 1b, the XRD pattern of Co<sub>2</sub>B-MoB<sub>2</sub>/CMO, a crystalline/amorphous heterointerface catalyst, presents broad peaks at  $2\theta \approx 34.0^{\circ}$  and  $45.4^{\circ}$ , corresponding to MoB<sub>2</sub> (JCPDS: 06-0682) and Co<sub>2</sub>B (JCPDS: 25-0241), respectively. The broadness of these peaks suggests poor crystallinity, likely due to the intense reduction process employed during synthesis [31]. The XRD spectra of Co<sub>2</sub>B-Co<sub>3</sub>(BO<sub>3</sub>)<sub>2</sub> and Co<sub>2</sub>B-MoB<sub>2</sub> align with the known patterns of  $Co_2B$  (JCPDS: 25-0241),  $Co_3(BO_3)_2$  (JCPDS: 25-0102), and MoB<sub>2</sub> (JCPDS: 06-0682) (Fig. S1a-b). As illustrated in Fig. 1c, Co<sub>2</sub>B-- $MoB_2/CMO$  exhibits a contact angle of 51.4°, which is significantly lower than that of  $Co_2B-Co_3(BO_3)_2$  (64.6°) and  $Co_2B-MoB_2$  (58.0°). These results indicate that Mo-doped Co<sub>2</sub>B-MoB<sub>2</sub>/CMO and Co<sub>2</sub>B-MoB<sub>2</sub> exhibit greater hydrophilicity than Co<sub>2</sub>B-Co<sub>3</sub>(BO<sub>3</sub>)<sub>2</sub> [32]. The enhanced hydrophilicity of Co<sub>2</sub>B-MoB<sub>2</sub>/CMO is expected to facilitate the efficient transport of BH<sub>4</sub> and H<sub>2</sub>O, promoting their activation and accelerating the hydrolytic dehydrogenation of NaBH<sub>4</sub> [33]. The porosity variations between Co<sub>2</sub>B-MoB<sub>2</sub>/CMO and Co<sub>2</sub>B-Co<sub>3</sub>(BO<sub>3</sub>)<sub>2</sub> were analyzed using N<sub>2</sub> adsorption-desorption isotherms. The Brunauer-Emmett-Teller (BET) analysis revealed specific surface areas of 43.6 and 45.8 m<sup>2</sup> g<sup>-1</sup> for the respective samples (Fig. 1d). The isotherms of both materials exhibit type-IV behavior with an H3 hysteresis loop, while the measured pore sizes were 20.6 nm and 18.2 nm (inset in Fig. 1d), confirming the formation of mesoporous structures [34,35]. These mesopores and ample surface area provide enhanced pathways for electron transfer and mass diffusion, which are crucial for catalytic activity [36]. Electron paramagnetic resonance (EPR) spectroscopy further investigated defect properties. As shown in Fig. 1e, pure CMO shows no detectable EPR signal, whereas Co<sub>2</sub>B-MoB<sub>2</sub>/CMO and Co<sub>2</sub>B-Co<sub>3</sub>(BO<sub>3</sub>)<sub>2</sub> exhibit distinct signals at g = 2.15 indicating the presence of Co defects. For semi-quantitative analysis of Co defect concentration, double integration (DIN) of the EPR signals was performed: the DIN intensity of Co<sub>2</sub>B-MoB<sub>2</sub>/CMO was normalized to 1.00, compared to 0.65 for Co<sub>2</sub>B-Co<sub>3</sub>(BO<sub>3</sub>)<sub>2</sub> and near-negligible intensity for pure CMO. This confirms Co<sub>2</sub>B-MoB<sub>2</sub>/CMO has the highest unpaired electron concentration and thus the richest Co defects [37,38]. These defects facilitate the

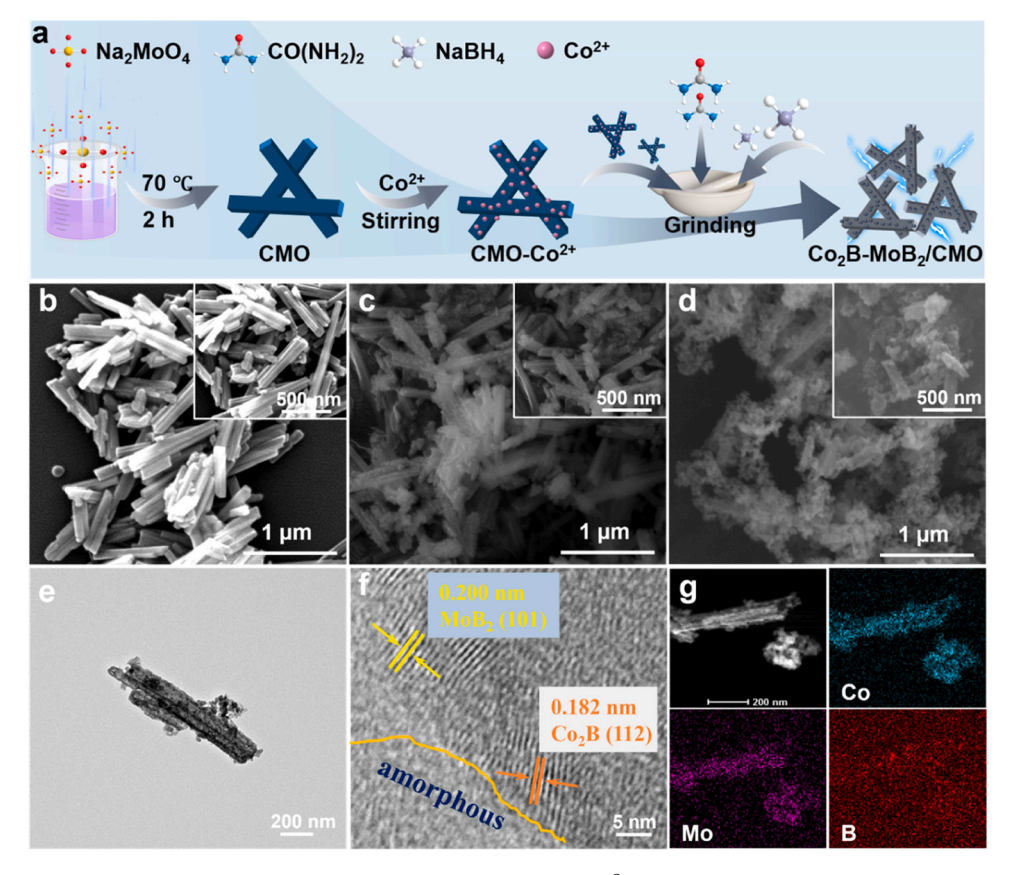


Fig. 2. (a) Schematic illustration of the synthesis process. SEM images of (b) CMO, (c) CMO-Co<sup>2+</sup>, and (d) Co<sub>2</sub>B-MoB<sub>2</sub>/CMO. (e) TEM and (f) HR-TEM of Co<sub>2</sub>B-MoB<sub>2</sub>/CMO. (g) HAADF-TEM images and the corresponding elemental mappings of Co<sub>2</sub>B-MoB<sub>2</sub>/CMO (Co, Mo and B).

dispersion and anchoring of metal nanoparticles (NPs) while modifying the electronic structure of  $\text{Co}_2\text{B-MoB}_2/\text{CMO}$ . The resulting electron-rich surface state is expected to enhance catalytic performance. The microstructures of the materials were further characterized using Raman spectroscopy. As depicted in Fig. 1f, the characteristic peaks at 334, 358, 852, and 933 cm<sup>-1</sup> are assigned to Co-O-Mo, O-Mo-O, and Mo-O-Co bonding in CMO, confirming its successful synthesis [39,40]. The

Raman spectra of  $Co_2B-MoB_2/CMO$  and  $Co_2B-Co_3(BO_3)_2$  display five peaks at 665, 608, 506, 466, and  $188~cm^{-1}$ . These characteristic peaks can be assigned to the fundamental Raman-active phonon modes  $(A_{1g}, F_{2g}, F_{2g}, F_{g}$  and  $F_{2g}$ , respectively) that are diagnostic of cobalt oxide phases [41]. Upon exposure to air, metal borides naturally oxidize. Consequently, the Raman spectra of  $Co_2B-MoB_2/CMO$  and  $Co_2B-Co_3(BO_3)_2$  primarily reflect peaks corresponding to their oxidized

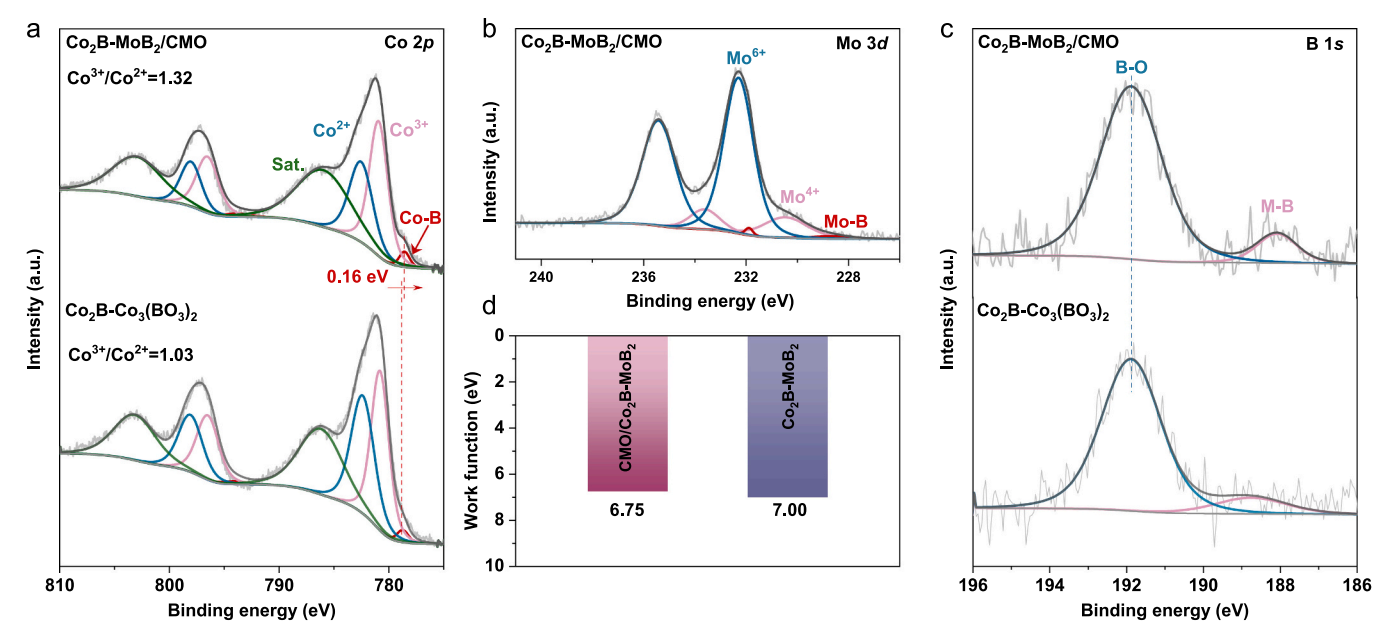


Fig. 3. High-resolution XPS spectra of (a) Co 2p, (b) Mo 3d, and (c) B 1 s for Co<sub>2</sub>B-MoB<sub>2</sub>/CMO and Co<sub>2</sub>B-Co<sub>3</sub>(BO<sub>3</sub>)<sub>2</sub>. (d) Work functions of the different catalysts.

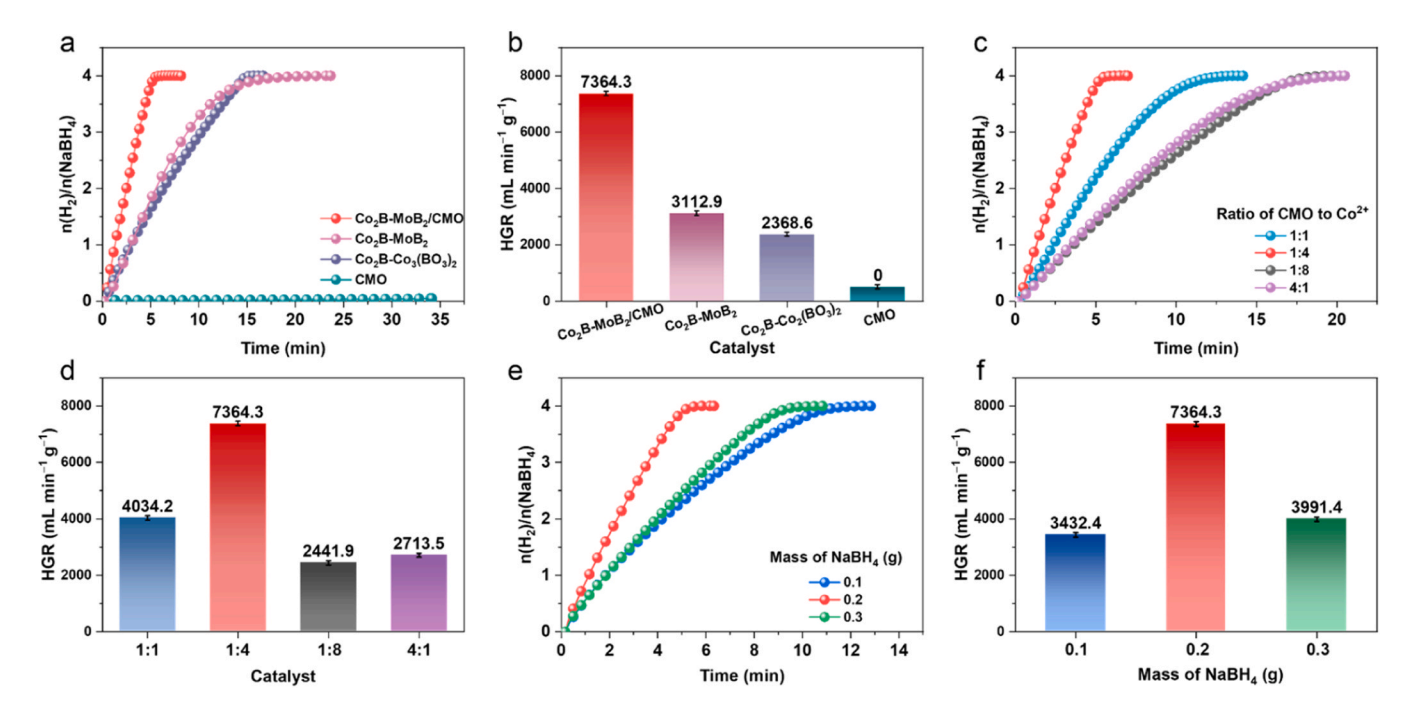


Fig. 4. (a) The temporal evolution of hydrogen production rates was systematically compared across various catalytic systems and (b) the corresponding HGR values. (c) Stoichiometric hydrogen evolution from 150 mM NaBH $_4$  + 0.4 wt% NaOH solution by Co $_2$ B-MoB $_2$ /CMO catalysts with varying ratios of CMO to Co at 25 °C and (d) the corresponding HGR values. (e) Co $_2$ B-MoB $_2$ /CMO prepared with different NaBH $_4$  dosages and (f) the corresponding HGR values. All catalytic evaluations were conducted in 150 mM NaBH $_4$  + 0.4 wt% NaOH solution at 25 °C.

species [42].

The target catalyst was synthesized using a chemical co-precipitation method followed by NaBH<sub>4</sub> reduction (Fig. 2a). Initially, CoMoO<sub>6</sub>·0.9 H<sub>2</sub>O (CMO) nanorods were prepared via the coprecipitation method. A specific amount of CMO nanorods was then immersed in an acetone solution containing varying concentrations of CoCl<sub>2</sub>·6 H<sub>2</sub>O to ensure uniform dispersion of CoCl<sub>2</sub>·6 H<sub>2</sub>O on the CMO nanorod surface. Subsequently, the resulting precursors were mixed with NaCl and urea, and the crystalline/amorphous Co<sub>2</sub>B-MoB<sub>2</sub>/CMO heterointerface catalysts were synthesized via solid-phase reduction using sodium borohydride. Herein, NaCl and urea respectively undertake critical regulatory roles: NaCl effectively suppresses the agglomeration of Co<sub>2</sub>B-MoB<sub>2</sub>/CMO nanoparticles by virtue of its high ionic strength, while urea slows down the reduction kinetic rate of NaBH<sub>4</sub> [43, 44]. This synergistic regulation of dispersion and reaction kinetics provides favorable conditions for the construction of crystalline/amorphous heterointerfaces. The morphological and surface properties of the synthesized materials were characterized using scanning electron microscopy (SEM). The SEM images reveal that the CMO nanorods possess a smooth and clean surface (Fig. 2b). As shown in Fig. 2c, large quantity of cobalt salts are firmly attached to the surface of the CMO nanorods. Following the sodium borohydride reduction reaction, the rod-like structure of the precursor is preserved, while numerous small-sized nanoparticles appear on the surface (Fig. 2d). Fig. S2a-b further illustrates that Co<sub>2</sub>B-Co<sub>3</sub>(BO<sub>3</sub>)<sub>2</sub> and Co<sub>2</sub>B-MoB<sub>2</sub> also contain a significant number of small-sized nanoparticles. Transmission electron microscopy (TEM) images (Fig. 2e) confirm that the nanorod structure of Co<sub>2</sub>B-Co<sub>3</sub>(BO<sub>3</sub>)<sub>2</sub> remains intact after the reduction process. Additionally, high-resolution TEM (HR-TEM) images (Fig. 2f) display well-defined lattice fringes of 0.182 nm and 0.200 nm, corresponding to Co<sub>2</sub>B (112) and MoB<sub>2</sub> (101) planes, respectively. Furthermore, a clear interface between the crystalline and amorphous phases is observed (Fig. 2c). The close integration of these three components forms a multi-hierarchical tandem structure, which plays a crucial role in optimizing the synergistic effects among them [45]. Elemental mapping obtained from X-ray energy-dispersive spectroscopy (EDS) (Fig. 2g)

confirms the uniform distribution of Co, Mo, and B atoms throughout the Co<sub>2</sub>B-MoB<sub>2</sub>/CMO catalyst.

X-ray photoelectron spectroscopy (XPS) was employed to characterize the oxidation states and spatial distribution of constituent elements in the catalytic material. The full-range spectrum (Fig. S3a) demonstrates the coexistence of Co, Mo, O, and B in the Co<sub>2</sub>B-MoB<sub>2</sub>/ CMO composite. High-resolution XPS spectra of the C 1 s region were analyzed using reference peaks for C-C (284.8 eV), C-O (286.0 eV), and C=O (288.9 eV) (Fig. S3b-c) [46,47]. The high-resolution Co 2p spectrum of Co<sub>2</sub>B-MoB<sub>2</sub>/CMO (Fig. 3a) exhibits four distinct peaks corresponding to Co-B (778.6 eV), Co<sup>3+</sup> (780.9 eV), Co<sup>2+</sup> (782.5 eV), and a satellite peak (786.0 eV) [48]. This surface oxide formation agrees well with the vibrational modes observed in Raman analysis. Notably, the Co<sup>3+</sup>/Co<sup>2+</sup> area ratio in Co<sub>2</sub>B-MoB<sub>2</sub>/CMO is 1.32, significantly higher than that in Co<sub>2</sub>B-Co<sub>3</sub>(BO<sub>3</sub>)<sub>2</sub> (1.03), suggesting a higher concentration of Co defects in Co<sub>2</sub>B-MoB<sub>2</sub>/CMO [49]. The Mo 3d XPS spectrum (Fig. 3b) displays two characteristic doublet peaks at binding energies of 232.33 eV ( $3d_{5/2}$ ) and 235.45 eV ( $3d_{3/2}$ ), which are diagnostic of Mo<sup>6+</sup> species in the material [50]. Additionally, two peaks at 230.43 eV and 233.65 eV, with an energy separation of 3.22 eV, correspond to Mo<sup>4+</sup> ions [51]. The B 1 s spectra of Co<sub>2</sub>B-MoB<sub>2</sub>/CMO and Co<sub>2</sub>B-Co<sub>3</sub>(BO<sub>3</sub>)<sub>2</sub> were deconvoluted into two peaks, corresponding to M-B and B-O bonds, confirming the formation of M-B alloys (Fig. 3c) [52]. The Co-B peak in Co<sub>2</sub>B-MoB<sub>2</sub>/CMO exhibits a negative shift of 0.16 eV compared to Co<sub>2</sub>B-Co<sub>3</sub>(BO<sub>3</sub>)<sub>2</sub>, suggesting that the increased Co defects enhance electronic interactions between Co<sub>2</sub>B and MoB<sub>2</sub>. This synergistic effect lowers the activation energy of the reaction, significantly enhancing the catalytic efficiency [44]. To further investigate the space charge transfer mechanism, ultraviolet photoelectron spectroscopy (UPS) was employed [53]. The work function (WF) difference, derived from UPS data (Fig. S4), determines the direction and feasibility of electron transfer [54]. The calculated work function for Co<sub>2</sub>B--MoB<sub>2</sub>/CMO is 6.75 eV, lower than that of Co<sub>2</sub>B-MoB<sub>2</sub> (7.00 eV). This decrease facilitates more efficient electron migration from bulk to surface regions, thereby promoting interfacial charge transfer with reactant species. This enhanced electron exchange with reactants improves the

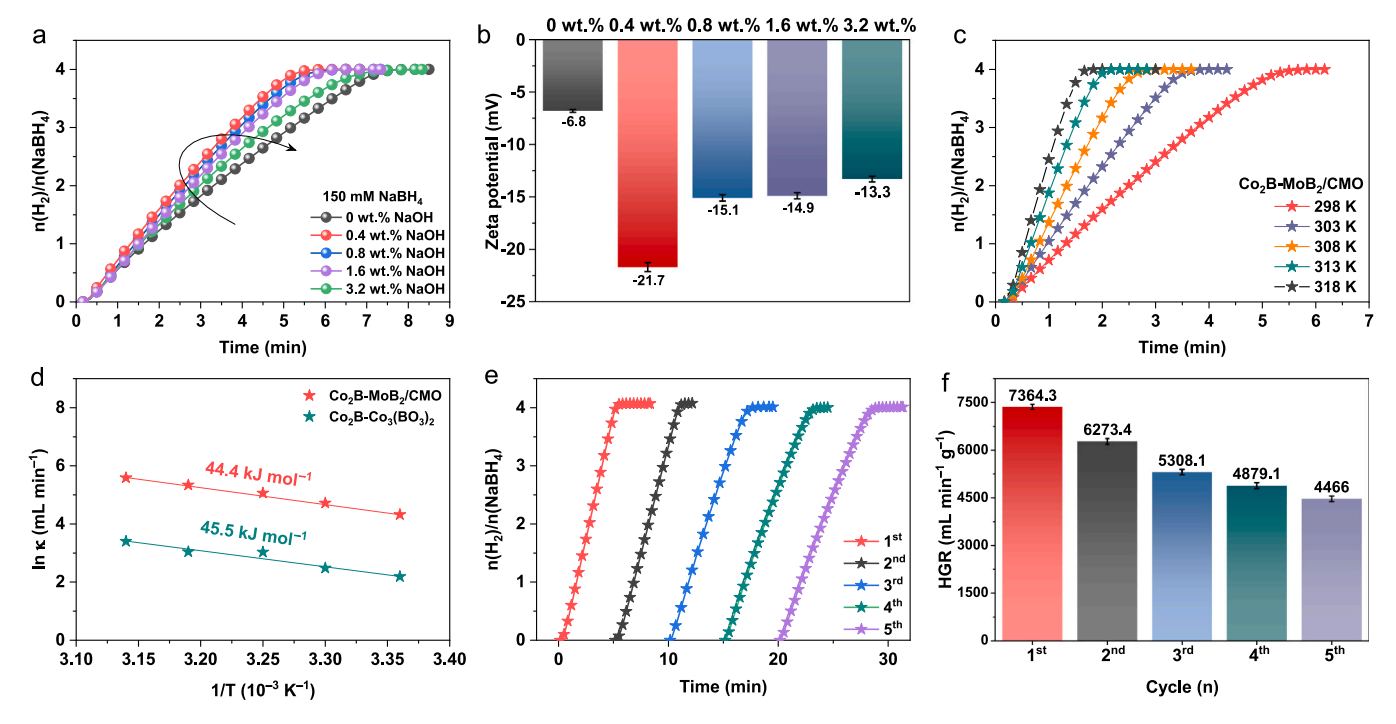


Fig. 5. (a) HGR as a function of NaOH concentration at fixed NaBH<sub>4</sub> (150 mM) and 25 °C, accompanied by (b) corresponding zeta potential measurements. (c) Temporal profiles of H<sub>2</sub> production at various temperatures (298–318 K). (d) Arrhenius plot derived from the temperature-dependent kinetic data in (c). (e) Cyclic stability assessment of the Co<sub>2</sub>B-MoB<sub>2</sub>/CMO catalyst conducted at 25 °C. (f) Summarized HGR from (e).

catalyst's dynamic performance, further facilitated by the introduction of the CMO carrier [55].

#### 3.2. Performance of catalyst for NaBH<sub>4</sub> hydrolysis

The catalytic hydrolysis performance of NaBH<sub>4</sub> was analyzed via the drained approach, with details provided in Fig. S5. Previous studies indicate that NaBH<sub>4</sub> undergoes weak self-decomposition in aqueous solution (Fig. S6a). Given that NaBH4 maintains stability in alkaline solutions (Fig. S6b), its reaction with catalysts allows controlled H2 release. The catalytic performance was quantified by evaluating the hydrogen production rates of different catalysts. As shown in Fig. 4a-b, the hydrogen generation rates followed this order: Co<sub>2</sub>B-MoB<sub>2</sub>/CMO  $> Co_2B-MoB_2 > Co_2B-Co_3(BO_3)_2 > CMO$ .  $Co_2B-MoB_2/CMO$  outperformed all other catalysts in terms of hydrolysis kinetics, displaying a superior hydrogen evolution rate of 7364.3 mL min<sup>-1</sup> g<sup>-1</sup>. The results suggest that Mo species function as promoters, playing a crucial role in enhancing the catalytic activity of NaBH<sub>4</sub> hydrolysis [12]. The influence of the CMO-to-Co<sup>2+</sup> mass ratio on catalytic performance was systematically examined to identify the optimal preparation conditions. The best performance was observed at a CMO/Co<sup>2+</sup> ratio of 1:4 (Fig. 4c-d). This corresponds to the EPR results, where the 1:4 ratio shows the strongest signal at g = 2.15, verifying that more Co defects correlate with superior catalytic performance. The metal content in the catalysts was determined via ICP-MS (Table S1). As a function of cobalt loading, the hydrogen production rate exhibited a volcano-like trend. The superior catalytic activity of Co<sub>2</sub>B-MoB<sub>2</sub>/CMO is primarily attributed to abundant defect sites and strong synergistic interactions between the crystalline and amorphous phases [56]. As shown in Fig. 4e-f, catalyst activity was also influenced by the amount of NaBH4 used. When 200 mg of NaBH<sub>4</sub> was used, complete dehydrogenation occurred within 5.6 min at 298 K. However, when the NaBH<sub>4</sub> amount increased to 300 mg, the catalytic activity of  $Co_2B\text{-}MoB_2/CMO$  decreased, likely due to partial structural degradation of the catalyst framework [57]. The influence of catalyst dosage on NaBH4 dehydrogenation kinetics was systematically investigated by varying the amount of Co<sub>2</sub>B-MoB<sub>2</sub>/CMO.

Optimal catalytic performance was achieved with 10 mg of  $\text{Co}_2\text{B-MoB}_2/\text{CMO}$ , which showed superior hydrogen evolution activity while maintaining economic viability (Fig. S7a-b).

NaOH, as a promoter, plays a crucial role in influencing the dehydrogenation activity of NaBH<sub>4</sub>. The hydrolysis rate of Co<sub>2</sub>B-MoB<sub>2</sub>/CMO was examined at varying NaOH concentrations to investigate its effect on catalytic performance. As shown in Fig. 5a, the hydrogen generation rate follows a volcano-like trend as NaOH concentration increases from 0 to 3.2 wt%. This suggests that an optimal NaOH concentration enhances NaBH<sub>4</sub> hydrolysis by providing OH<sup>-</sup> ions, which subsequently facilitate reactant adsorption and activation, leading to accelerated reaction rates. However, excessively high NaOH concentration significantly increases the reaction solution's viscosity and alkalinity, and the elevated viscosity inhibits reactant mass transfer. Zeta potential measurements further support this observation, exhibiting a trend similar to the volcano plot with increasing NaOH concentration (Fig. 5b). This confirms that NaOH concentration plays a key role in optimizing catalytic performance. To assess the effect of NaBH<sub>4</sub> concentration, experiments were conducted by increasing NaBH<sub>4</sub> concentration from 100 to 250 mM. The results indicate that the hydrogen generation rate remains unchanged, demonstrating zero-order kinetics to NaBH<sub>4</sub> concentration (Fig. S8) [58]. To evaluate the influence of reaction temperature on catalyst performance, kinetic studies were performed within the range of 298-318 K. As shown in Fig. 5c, the hydrogen generation rate of Co<sub>2</sub>B-MoB<sub>2</sub>/CMO increases significantly with temperature. The activation energy for NaBH<sub>4</sub> hydrolysis catalyzed by Co<sub>2</sub>B-MoB<sub>2</sub>/CMO was determined to be 44.4 kJ mol<sup>-1</sup> from the Arrhenius plot (Fig. 5d). This value is lower than that of  $Co_2B-Co_3(BO_3)_2$  (45.5 kJ  $mol^{-1}$ ) and compares favorably with most reported values in the literature (Table S2). This lower activation energy indicates a significant improvement in reaction kinetics, primarily due to abundant defects, which effectively reduce reaction energy barriers and enhance catalytic performance [59]. Reusability is a critical factor for practical catalyst applications. Durability tests of Co<sub>2</sub>B-MoB<sub>2</sub>/CMO were conducted at 25 °C over five consecutive cycles. As shown in Fig. 5e-f, the H2 generation rate experiences only a slight decline. This is primarily attributable to the

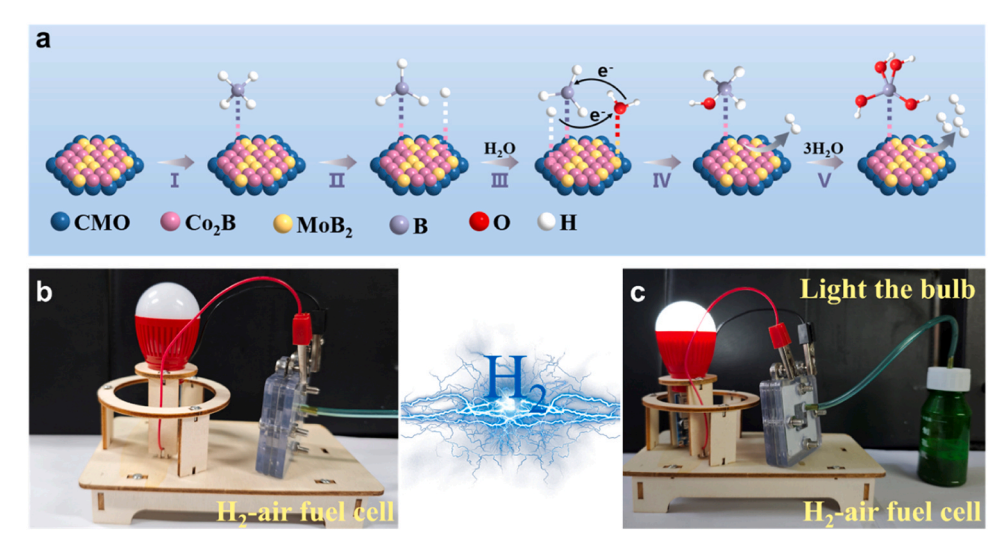


Fig. 6. (a) Proposed catalytic mechanism of the Co<sub>2</sub>B-MoB<sub>2</sub>/CMO catalyst for hydrogen generation via alkaline NaBH<sub>4</sub> hydrolysis. (b-c) Model of a fuel cell small light equipped with NaBH<sub>4</sub> and the Co<sub>2</sub>B-MoB<sub>2</sub>/CMO catalyst.

adsorption of the borate ions generated during the reaction onto the catalyst surface, resulting in the partial coverage of active sites [60]. Post-cycle SEM, XRD and XPS (Fig. S9 and Fig. S10) characterizations of Co<sub>2</sub>B-MoB<sub>2</sub>/CMO confirm that its composition and crystal structure remains stable, further emphasizing its high stability and potential for long-term application.

#### 3.3. Catalytic mechanism analysis

Fig. 6a illustrates a plausible Michaelis–Menten mechanism [61,62] for NaBH<sub>4</sub> hydrolysis catalyzed by Co<sub>2</sub>B-MoB<sub>2</sub>/CMO. Initially, BH<sub>4</sub> is adsorbed onto the surface of Co2B. Due to the electronegativity difference, the hydridic hydrogen in the B-H bond of BH<sub>4</sub> dissociates into H<sup>-</sup> and BH<sub>3</sub>. The generated H<sup>-</sup> on the Co<sub>2</sub>B surface then rapidly reacts with a proton (H<sup>+</sup>) from H<sub>2</sub>O, forming H<sub>2</sub> molecules. Simultaneously, the remaining -OH combines with BH3, generating the intermediate BH<sub>3</sub>OH<sup>-</sup>. As the reaction progresses, H atoms from BH<sub>3</sub>OH<sup>-</sup> continue to adsorb onto Co<sub>2</sub>B. Eventually, the remaining hydrogen atoms in the borohydride species are substituted by OH- ions, ultimately forming B(OH)<sub>4</sub>. In this study, we elucidated the potential mechanism of Co<sub>2</sub>B-MoB<sub>2</sub>/CMO-catalyzed NaBH<sub>4</sub> hydrolysis and successfully demonstrated an innovative experiment in which the hydrogen gas produced from this reaction powered a fuel cell. The experiment in which NaBH<sub>4</sub> is hydrolyzed to produce hydrogen and light a small lamp, as shown in Fig. 6b-c, visually demonstrates the key role of high-performance catalysts in hydrogen energy applications. The success of this experiment provides a strong scientific basis and application demonstration for the development of high-performance catalysts to promote hydrogen energy technology towards practical application.

## 4. Conclusions

In summary, we have successfully prepared the  $Co_2B\text{-}MoB_2/CMO$  catalyst using a chemical co-precipitation method and  $NaBH_4$  reduction treatment. Benefitting from the structural and compositional merits, the synthesized  $Co_2B\text{-}MoB_2/CMO$  samples exhibit excellent sodium borohydride hydrolysis performance with hydrogen production rates as high as 7364.3 mL min $^{-1}$  g $^{-1}$ , which exceeds most reported catalysts. Experiments and characterization analyses indicate that the superior catalytic performance of this material is mainly attributed to two factors: first, the rapid ion conduction and electron-proton transport efficiency at the interface between its crystalline and amorphous states; second, the introduction of cobalt defects, which improves the electronic structure

and accelerates ion transfer speed. In addition, this study not only revealed the potential mechanism of  $Co_2B$ -Mo $B_2$ /CMO catalysts to promote the hydrolysis of NaBH4, but also successfully used the generated hydrogen for fuel cells, thus verifying the effectiveness of NaBH4 as a hydrogen storage medium and its potential for energy conversion applications.

#### CRediT authorship contribution statement

**Bin Wu:** Data curation, Funding acquisition. **Luyan Shi:** Writing – original draft, Methodology. **Chenxi Shang:** Methodology, Investigation. **Ke Zhu:** Data curation. **Fengli Wei:** Methodology, Data curation. **Tayirjan Taylor Isimjan:** Writing – review & editing. **Xiulin Yang:** Writing – review & editing, Supervision.

#### **Declaration of Competing Interest**

The authors declare that they have no known competing financial interests or personal relationships that could have appeared to influence the work reported in this paper.

### Acknowledgements

This work has been supported by the National Natural Science Foundation of China (No. 21965005, 52363028), Natural Science Foundation of Guangxi Province (2021GXNSFAA076001), Guangxi Technology Base and Talent Subject (GUIKE AD23023004, GUIKE AD20297039), and Key Laboratory of Applied Surface and Colloid Chemistry (Shaanxi Normal University), Ministry of Education, P. R. China.

#### Appendix A. Supporting information

Supplementary data associated with this article can be found in the online version at doi:10.1016/j.colsurfa.2025.138947.

#### **Data Availability**

The data that has been used is confidential.

#### References

 M. Zhang, J. Guan, Y. Tu, S. Wang, D. Deng, Highly efficient conversion of surplus electricity to hydrogen energy via polysulfides redox, Innovation 2 (2021) 100144.

- [2] Y. Jia, B. Han, J. Wang, S. Yuan, L. Tang, Z. Zhang, Y. Zou, L. Sun, Y. Du, L. Chen, X. Xiao, Inducing one-step dehydrogenation of magnesium borohydride via confinement in robust dodecahedral nitrogen-doped porous carbon scaffold, Adv. Mater. 36 (2024) 2406152.
- [3] M. Cai, H. Shi, Y. Zhang, J. Qu, H. Wang, Y. Guo, K. Du, W. Li, B. Deng, D. Wang, H. Yin, Rechargeable Zn-H<sub>2</sub>O hydrolysis battery for hydrogen storage and production, Angew. Chem. Int. Ed. 63 (2024) e202404025.
- [4] S. Rathod, D. Gajjar, K.K. Joshi, P. Pataniya, C.K. Sumesh, S. Kapatel, Catalytic hydrogen production via NaBH<sub>4</sub> hydrolysis: role of WO<sub>3</sub> nanopellets, Renew. Energy 248 (2025) 123156.
- [5] C.-L. Hsueh, C.-H. Liu, B.-H. Chen, M.-S. Lee, C.-Y. Chen, Y.-W. Lu, F. Tsau, J.-R. Ku, A novel design of solid-state NaBH<sub>4</sub> composite as a hydrogen source for 2W PEMFC applications, J. Power Sources 196 (2011) 3530–3538.
- [6] S.-C. Li, F.-C. Wang, The development of a sodium borohydride hydrogen generation system for proton exchange membrane fuel cell, Int. J. Hydrog, Energy 41 (2016) 3038–3051.
- [7] B.H. Liu, Z.P. Li, A review: Hydrogen generation from borohydride hydrolysis reaction, J. Power Sources 187 (2009) 527–534.
- [8] F. Yang, J. Ruan, T. Li, Y. Zou, C. Xiang, F. Xu, L. Sun, Hydrolysis of sodium borohydride using a highly stable catalyst of ruthenium nanoparticles supported by cobalt–nickel hydroxide-coated nickel foam, J. Alloy. Compd. 926 (2022) 166902.
- [9] N. Wang, Q. Sun, T. Zhang, A. Mayoral, L. Li, X. Zhou, J. Xu, P. Zhang, J. Yu, Impregnating subnanometer metallic nanocatalysts into self-pillared zeolite nanosheets, J. Am. Chem. Soc. 143 (2021) 6905–6914.
- [10] K. Mori, K. Miyawaki, H. Yamashita, Ru and Ru–Ni nanoparticles on TiO<sub>2</sub> support as extremely active catalysts for hydrogen production from ammonia–borane, ACS Catal. 6 (2016) 3128–3135.
- [11] W. Chen, W. Zheng, J. Cao, W. Fu, G. Qian, D. Chen, X. Zhou, X. Duan, Atomic insights into robust Pt-PdO interfacial site-boosted hydrogen generation, ACS Catal. 10 (2020) 11417–11429.
- [12] Y. Meng, Q. Sun, T. Zhang, J. Zhang, Z. Dong, Y. Ma, Z. Wu, H. Wang, X. Bao, Q. Sun, J. Yu, Cobalt-promoted noble-metal catalysts for efficient hydrogen generation from ammonia borane hydrolysis, J. Am. Chem. Soc. 145 (2023) 5486–5495
- [13] Q. Yao, Y. Ding, Z.-H. Lu, Noble-metal-free nanocatalysts for hydrogen generation from boron- and nitrogen-based hydrides, Inorg. Chem. Front. 7 (2020) 3837–3874.
- [14] J.-M. Yan, X.-B. Zhang, S. Han, H. Shioyama, Q. Xu, Iron-nanoparticle-catalyzed hydrolytic dehydrogenation of ammonia borane for chemical hydrogen storage, Angew. Chem. Int. Ed. 47 (2008) 2287–2289.
- [15] H. Wu, M. Wu, B. Wang, X. Yong, Y. Liu, B. Li, B. Liu, S. Lu, Interface electron collaborative migration of Co–Co<sub>3</sub>O<sub>4</sub>/carbon dots: Boosting the hydrolytic dehydrogenation of ammonia borane, J. Energy Chem. 48 (2020) 43–53.
- [16] A. Bulut, M. Yurderi, İ.E. Ertas, M. Celebi, M. Kaya, M. Zahmakiran, Carbon dispersed copper-cobalt alloy nanoparticles: a cost-effective heterogeneous catalyst with exceptional performance in the hydrolytic dehydrogenation of ammoniaborane, Appl. Catal. B Environ. Energy 180 (2016) 121–129.
- [17] Y. Kang, B. Jiang, J. Yang, Z. Wan, J. Na, Q. Li, H. Li, J. Henzie, Y. Sakka, Y. Yamauchi, T. Asahi, Amorphous alloy architectures in pore walls: mesoporous amorphous NiCoB alloy spheres with controlled compositions via a chemical reduction, ACS Nano 14 (2020) 17224–17232.
- [18] X. Zhang, Y. Zhao, X. Jia, Y. Zhao, L. Shang, Q. Wang, G.I.N. Waterhouse, L.-Z. Wu, C.-H. Tung, T. Zhang, Silica-protected ultrathin Ni<sub>3</sub>FeN nanocatalyst for the efficient hydrolytic dehydrogenation of NH<sub>3</sub>BH<sub>3</sub>, Adv. Energy Mater. 8 (2018) 1702780
- [19] C.-C. Hou, Q. Li, C.-J. Wang, C.-Y. Peng, Q.-Q. Chen, H.-F. Ye, W.-F. Fu, C.-M. Che, N. López, Y. Chen, Ternary Ni-Co-P nanoparticles as noble-metal-free catalysts to boost the hydrolytic dehydrogenation of ammonia-borane, Energy Environ. Sci. 10 (2017) 1770–1776.
- [20] Y. Wang, P. Wang, J. Yuan, N. Song, X. An, X. Ma, J. Feng, B. Xi, S. Xiong, Binary sulfiphilic nickel boride on boron-doped graphene with beneficial interfacial charge for accelerated Li–S dynamics, Small 19 (2023) 2208281.
- [21] J. Li, X. Hong, Y. Wang, Y. Luo, P. Huang, B. Li, K. Zhang, Y. Zou, L. Sun, F. Xu, F. Rosei, S.P. Verevkin, A.A. Pimerzin, Encapsulated cobalt nanoparticles as a recoverable catalyst for the hydrolysis of sodium borohydride, Energy Storage Mater. 27 (2020) 187–197.
- [22] F. Li, J. Li, L. Chen, Y. Dong, P. Xie, Q. Li, Preparation of CoB nanoparticles decorated PANI nanotubes as catalysts for hydrogen generation from NaBH<sub>4</sub> hydrolysis, J. Taiwan Inst. Chem. E. 122 (2021) 148–156.
- [23] H. Tian, K. Zhang, X. Feng, J. Chen, Y. Lou, Self-supported CoMoO<sub>4</sub>/NiFe-LDH core–shell nanorods grown on nickel foam for enhanced electrocatalysis of oxygen evolution, Dalton Trans. 51 (2022) 13762–13770.
- [24] P. Zhou, Z. Li, Y. Zhao, B. Zhao, W. Jiang, X. Chen, J. Wang, R. Yang, C. Zuo, Hybridization of bimetallic cobalt-molybdenum oxide multihole nanosheets with selenium adulteration as advanced bifunctional electrocatalysts for boosting overall water splitting, J. Colloid Interface Sci. 675 (2024) 302–312.
- [25] Y. Zhou, Y. Liang, Z. Wu, X. Wang, R. Guan, C. Li, F. Qiao, J. Wang, Y. Fu, J.-B. Baek, Amorphous/crystalline heterostructured nanomaterials: an emerging platform for electrochemical energy storage, Small 21 (2025) 2411941.
- [26] Z. Liang, Q. Li, F. Li, S. Zhao, X. Xia, Hydrogen generation from hydrolysis of NaBH<sub>4</sub> based on high stable NiB/NiFe<sub>2</sub>O<sub>4</sub> catalyst, Int. J. Hydrog. Energy 42 (2017) 3971–3980.
- [27] J. Hou, Y. Sheng, D. Bi, N. Chen, Q. Lai, Y. Liang, Interface engineering of crystalline-amorphous heterostructures with strong electronic interactions for efficient alkaline overall water splitting, J. Alloy. Compd. 977 (2024) 173447.

- [28] K. Zhang, Q. Su, W. Shi, Y. Lv, R. Zhu, Z. Wang, W. Zhao, M. Zhang, S. Ding, S. Ma, G. Du, B. Xu, Copious dislocations defect in amorphous/crystalline/amorphous sandwiched structure P–NiMoO<sub>4</sub> electrocatalyst toward enhanced hydrogen evolution reaction, ACS Nano 18 (2024) 3791–3800.
- [29] C. Shang, L. Shi, S. Zhou, S. Muhammad, T.T. Isimjan, H. Hu, X. Yang, Interface engineering of Co<sub>2</sub>B–MoO<sub>3</sub>/MOF heterojunctions with rich cobalt defects for highly enhanced NaBH<sub>4</sub> hydrolysis, Inorg. Chem. Front. 11 (2024) 7142–7151.
- [30] J.-F. Hou, J.-F. Gao, L.-B. Kong, Boosting the performance of cobalt molybdate nanorods by introducing nanoflake-like cobalt boride to form a heterostructure for aqueous hybrid supercapacitors, J. Colloid Interface Sci. 565 (2020) 388–399.
- [31] J.-F. Hou, J.-F. Gao, L.-B. Kong, Interfacial engineering in crystalline cobalt tungstate/amorphous cobalt boride heterogeneous nanostructures for enhanced electrochemical performances, ACS Appl. Electron. Mater. 3 (2020) 11470–11479.
- [32] J. He, A. Bhargav, A. Manthiram, Molybdenum boride as an efficient catalyst for polysulfide redox to enable high-energy-density lithium-sulfur batteries, Adv. Mater. 32 (2020) 2004741.
- [33] P. Li, Y. Huang, Q. Huang, R. Chen, J. Li, S. Tian, Cobalt phosphide with porous multishelled hollow structure design realizing promoted ammonia borane dehydrogenation: elucidating roles of architectural and electronic effect, Appl. Catal. B Environ. Energy 313 (2022) 121444.
- [34] X. Hou, C. Yu, T. Ni, S. Zhang, J. Zhou, S. Dai, L. Chu, M. Huang, Constructing amorphous/crystalline NiFe-MOF@NiS heterojunction catalysts for enhanced water/seawater oxidation at large current density, Chin. J. Catal. 61 (2024) 192–204.
- [35] H. Chu, Y. Wu, S. Qiu, C. Shao, Y. Xia, Y. Zou, B. Li, K. Dai, L. Sun, Carboxylate trapping engineering to fabricate monodispersed dual-atom iron sites for efficient oxygen reduction, Inorg. Chem. Front 11 (2024) 2260–2271.
- [36] K. Pradeep, A.A. Jeffery, A.P. Sundaresan, R. Gunaseelan, S. Rajendran, P. E. Karthik, Y.-H. Ahn, N.C. Sagaya, Selvam, Impact of catalyst engineering on the durability performance of self-supported catalysts in anion exchange membrane water electrolyzers: recent advances and perspectives, J. Mater. Chem. A 13 (2025) 14510–14539.
- [37] L. Wang, J. Huang, Z. Huang, H. Li, T. Taylor Isimjan, X. Yang, Revealing dynamic structural evolution of V and P co-doping-induced Co defects as large-current water oxidation catalyst, Chem. Eng. J. 472 (2023) 144924.
- [38] L. Hou, Z. Zhang, X. Cui, C. Sun, M.G. Kim, H. Jang, Z. Li, X. Liu, g-C<sub>3</sub>N<sub>4</sub>-mediated synthesis of Ru crystalline/amorphous heterostructures on N-doped carbon for efficient and chloride-resistant alkaline HER, Adv. Funct. Mater. (2025) e17551, https://doi.org/10.1002/adfm.202517551.
- [39] X. Ma, B. Wei, M. Yuan, J. Li, S. Liang, Y. Wu, D. Dai, L. Xu, Self-supported phosphorus-doped CoMoO<sub>4</sub> rod bundles for efficient hydrogen evolution, J. Mater. 55 (2020) 6502–6512.
- [40] P.M. Ette, A. Chithambararaj, A.S. Prakash, K. Ramesha, MoS<sub>2</sub> nanoflower-derived interconnected CoMoO<sub>4</sub> nanoarchitectures as a stable and high rate performing anode for lithium-ion battery applications, ACS Appl. Mater. Interfaces 12 (2020) 11511–11521.
- [41] Z. Deng, C. Ma, Z. Li, Y. Luo, L. Zhang, S. Sun, Q. Liu, J. Du, Q. Lu, B. Zheng, X. Sun, High-efficiency electrochemical nitrate reduction to ammonia on a Co<sub>3</sub>O<sub>4</sub> nanoarray catalyst with cobalt vacancies, ACS Appl. Mater. Interfaces 14 (2022) 46595–46602
- [42] J. Masa, I. Sinev, H. Mistry, E. Ventosa, M. de la Mata, J. Arbiol, M. Muhler, B. Roldan Cuenya, W. Schuhmann, Ultrathin high surface area nickel boride (NiB) nanosheets as highly efficient electrocatalyst for oxygen evolution, Adv. Energy Mater. 7 (2017) 1700381.
- [43] M.M. Durano, A.H. Tamboli, H. Kim, Cobalt oxide synthesized using urea precipitation method as catalyst for the hydrolysis of sodium borohydride, Colloids Surf. A Physicochem. Eng. Asp. 520 (2017) 355–360.
- [44] S. Zhou, L. Cheng, Y. Liu, J. Tian, C. Niu, W. Li, S. Xu, T.T. Isimjan, X. Yang, Highly active and robust catalyst: Co<sub>2</sub>B–Fe<sub>2</sub>B heterostructural nanosheets with abundant defects for hydrogen production, Inorg. Chem. 63 (2024) 2015–2023.
- [45] B. Lin, J. Chen, R. Yang, S. Mao, M. Qin, Y. Wang, Multi-hierarchical cobalt-based electrocatalyst towards high rate H<sub>2</sub> production, Appl. Catal. B Environ. Energy 316 (2022) 121666.
- [46] F. He, A. Meng, B. Cheng, W. Ho, J. Yu, Enhanced photocatalytic H<sub>2</sub>-production activity of WO<sub>3</sub>/TiO<sub>2</sub> step-scheme heterojunction by graphene modification, Chin. J. Catal. 41 (2020) 9–20.
- [47] C. Zhang, C. Xiang, X. Liu, S. Fan, J. Yan, L. Sun, Y. Zou, X. Liu, Mechanism insight into "on-off" control for demand-based H<sub>2</sub> evolution completely from water over NiO/CNT nanocatalyst, Appl. Catal. B Environ. Energy 371 (2025) 125204.
- [48] F. Yang, C. Xiang, S. Fang, F. Xu, L. Sun, C.Y. Shen, Y. Zou, Synthesis and catalytic performance of nanoflower-like Ru@CoAl-LDH composite catalyst for NaBH<sub>4</sub> hydrolysis, J. Alloy. Compd. 945 (2023) 169280.
- [49] X. Liu, L. Zhao, H. Xu, Q. Huang, Y. Wang, C. Hou, Y. Hou, J. Wang, F. Dang, J. Zhang, Tunable cationic vacancies of cobalt oxides for efficient electrocatalysis in Li-O<sub>2</sub> batteries, Adv. Energy Mater. 10 (2020) 2001415.
- [50] K. Dastafkan, S. Wang, C. Rong, Q. Meyer, Y. Li, Q. Zhang, C. Zhao, Cosynergistic molybdate oxo-anionic modification of FeNi-based electrocatalysts for efficient oxygen evolution reaction, Adv. Funct. Mater. 32 (2022) 2107342.
- [51] Y. Li, S. Zhang, M. Ma, X. Mu, Y. Zhang, J. Du, Q. Hu, B. Huang, X. Hua, G. Liu, E. Xie, Z. Zhang, Manganese-doped nickel molybdate nanostructures for highperformance asymmetric supercapacitors, Chem. Eng. J. 372 (2019) 452–461.
- [52] Z. Li, P. Li, X. Meng, Z. Lin, R. Wang, The interfacial electronic engineering in binary sulfiphilic cobalt boride heterostructure nanosheets for upgrading energy density and longevity of lithium-sulfur batteries, Adv. Mater. 33 (2021) 2102338.
- [53] L. Fu, Y. Kang, H.N. Nam, K. Wang, Z. Zhou, Y. Zhao, Q.M. Phung, K. Wu, Y. Asakura, J. Zhou, Y. Yamauchi, Harnessing work function modulation for

- hydrogen evolution catalysis in mesoporous bimetallic Pt-M alloys: the role of mesopores in work function optimization, Adv. Sci. 12 (2025) e05464.
- [54] J. Kim, H. Kim, W.-J. Lee, B. Ruqia, H. Baik, H.-S. Oh, S.-M. Paek, H.-K. Lim, C. H. Choi, S.-I. Choi, Theoretical and experimental understanding of hydrogen evolution reaction kinetics in alkaline electrolytes with Pt-based core-shell nanocrystals, J. Am. Chem. Soc. 141 (2019) 18256–18263.
- [55] Y. Song, M. Sun, S. Zhang, X. Zhang, P. Yi, J. Liu, B. Huang, M. Huang, L. Zhang, Alleviating the work function of vein-Like Co<sub>X</sub>P by Cr doping for enhanced seawater electrolysis, Adv. Funct. Mater. 33 (2023) 2214081.
- [56] A.K. Kar, R. Sarkar, A.K. Manal, R. Kumar, S. Chakraborty, R. Ahuja, R. Srivastava, Unveiling and understanding the remarkable enhancement in the catalytic activity by the defect creation in UIO-66 during the catalytic transfer hydrodeoxygenation of vanillin with isopropanol, Appl. Catal. B Environ. Energy 325 (2023) 122385.
- [57] J. Long, Q. Yao, X. Zhang, H. Wu, Z.-H. Lu, Defects engineering of metal-organic framework immobilized Ni-La(OH)<sub>3</sub> nanoparticles for enhanced hydrogen production, Appl. Catal. B Environ. Energy 320 (2023) 121989.
- [58] J. Yang, Z. Yang, J. Li, H. Gang, D. Mei, D. Yin, R. Deng, Y. Zhu, X. Li, N. Wang, S. M. Osman, Y. Yamauchi, Engineering a hollow bowl-like porous carbon-confined Ru–MgO hetero-structured nanopair as a high-performance catalyst for ammonia borane hydrolysis, Mater. Horiz. 11 (2024) 2032–2040.
- [59] S. Gao, S. Zhao, X. Tang, L. Sun, Q. Li, H. Yi, Research on the application of defect engineering in the field of environmental catalysis, Green. Energy Environ. 24 (2024) 00244–00249.
- [60] H. Chu, G. Li, C. Liu, C. Cui, Y. Li, S. Qiu, Y. Xia, Y. Zou, F. Xu, L. Sun, Ruthenium-based high-entropy alloys expediting hydrogen evolution through catalytic hydrolysis of ammonia borane, ACS Appl. Energy Mater. 7 (2024) 9625–9633.
- [61] Q. Guo, X. Wang, F. Yang, S. Zhou, K. Wei, Y. Zhang, L. Sun, S. Sun, H. Liu, J. An, Y. Sun, P. Shen, Y. Li, Pt single-atomic-site loaded on borate anion-intercalated Co (OH)<sub>2</sub> nanoflakes for enhanced hydrogen generation dynamics of NaBH<sub>4</sub> hydrolysis, Chem. Eng. J. 516 (2025) 164141.
- [62] S. Zhou, Q. Yang, Y. Liu, L. Cheng, T. Taylor Isimjan, J. Tian, X. Yang, Electronic metal-support interactions for defect-induced Ru/Co-Sm<sub>2</sub>O<sub>3</sub> mesosphere to achieve efficient NaBH<sub>4</sub> hydrolysis activity, J. Catal. 433 (2024) 115491.